ANALYZING TOMOGRAPHIC SAR DATA OF A FOREST WITH RESPECT TO FREQUENCY, POLARIZATION, AND FOCUSING TECHNIQUE

Othmar Frey and Erich Meier

Remote Sensing Laboratories
University of Zurich, Switzerland

ABSTRACT

In this paper, two fully-polarimetric tomographic SAR data sets of a forested area, at L-band and P-band, are analyzed with respect to the localization of scattering sources and scattering mechanisms. In particular, the 3D SAR data is examined regarding the performance of three different tomographic focusing techniques multilook standard beamforming, robust Capon beamforming, and MUSIC, as well as for both, the two frequency bands and the different polarimetric channels.

***Index Terms*—** SAR Tomography, Multibaseline SAR, Beamforming, Capon, MUSIC, E-SAR, L-Band, P-Band

1. INTRODUCTION

Research towards improving the knowledge about the back-scattering behavior of forests with the goal of estimating biophysical parameters by means of synthetic aperture radar (SAR) tomography has become a major topic within the SAR remote sensing community. With three prospective space-borne SAR remote sensing missions, BIOMASS, at P-band, Tandem-L and DESDynI, both at L-band, these frequency bands have even gained in importance.

In September 2006, an airborne SAR campaign has been flown by the German Aerospace Center's E-SAR system over a test site in Switzerland [1], where two fully polarimetric tomographic data sets (P-band and L-band) of a partially forested area have been taken (see Table 1).

In this paper, the processing approach is sketched and excerpts from the data analysis are presented. In particular, we have (1) included a full three-dimensional image of the forest obtained from the L-band tomographic data set and having applied the Multiple Signal Classification method (see Fig. 1) for focusing in the normal direction; (2) the tomographic focusing performance is shown for both wavelengths and the three focusing methods, respectively, (see Fig. 2), (3) vertical profiles of the back-scattering amplitude for both the P-band and the L-band data set are given (see Fig. 3), as well as corresponding reference data obtained from airborne laser scanning (ALS) (see Fig. 4). (4) Finally, an entropy/α scatter plot is presented for different height levels within the forest volume (see Fig. 5).

	P-band	L-band
Carrier frequency	350 MHz	1.3 GHz
Chirp bandwidth	70 MHz	94 MHz
Sampling rate	100 MHz	100 MHz
PRF	500 Hz	400 Hz
Ground speed	90 m/s	90 m/s
No. of data tracks	11+1	16+1
Nominal track spacing d_n	57 m	14 m
Horizontal baselines	40 m	10 m
Vertical baselines	40 m	10 m
Synthetic aperture in normal direction L	570 m	210 m
Nominal resolution in normal direction δ_n	3 m	2 m
Approx. unambiguous height H	30 m	30 m

Table 1. E-SAR system specifications and nominal parameters of the tomographic acquisition patterns.
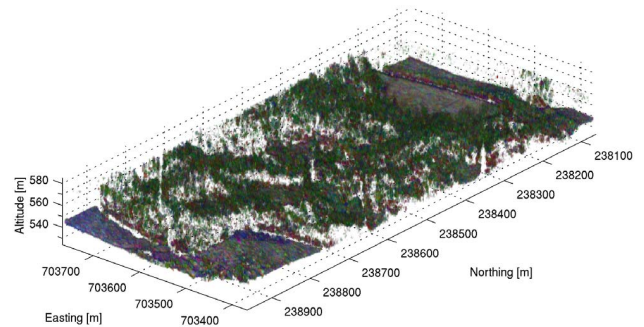
Fig. 1. Tomographic image (3D voxel plot) of a partially forested area obtained from combined TDBP and MUSIC beamforming of polarimetric airborne repeat-pass multibaseline SAR data at L-band. Each channel has been scaled individually. Red (HH), green (HV), blue (VV). Low intensity = high transparency of the voxel.

2. TOMOGRAPHIC FOCUSING

A modified time-domain tomographic processing approach is pursued to obtain a three-dimensional image of a par-

tially forested area: namely, a combination of standard time-domain back-projection (TDBP) processing for azimuth focusing [2] and time-domain multilook-based methods for tomographic focusing in the normal direction.

2.1. Multilook Standard Beamforming (MLBF)

The standard multilook beamforming approach has been applied using the TDBP-based approach described in [3].

2.2. Multiple Signal Classification (MUSIC)

In the following, the main steps to compute the location of the scatterers based on MUSIC [4] are given:
(1) Calculate the sample covariance matrix $\mathbf{R}$. (2) Calculate the eigen-decomposition of the sample covariance matrix $\mathbf{R} = \mathbf{UDU}^H$. (3) Permute the elements of the matrices such that the eigenvalues in $\mathbf{D}$ are sorted in nonincreasing order: $\gamma_1 \geq \gamma_2 \geq ... \geq \gamma_K$; the matrix of eigenvectors $\mathbf{U}$ is adjusted accordingly. (4) Set a threshold for the eigenvalue that separates the signal- and the noise-subspace, respectively. (5) Estimate the locations of the sources by evaluating

$$\hat{P}_M = \frac{1}{\mathbf{a}^H \mathbf{GG}^H \mathbf{a}} \qquad (1)$$

where $G = [\mathbf{u}_{p+1}...\mathbf{u}_K]$ contains the eigenvectors that span the noise space, and $\mathbf{a}$ is the steering vector.

2.3. Robust Capon Beamforming (RCB)

While the MUSIC algorithm possesses an inherent robustness against steering vector errors, as has been shown in [5], in the case of the Capon beamformer, an improved resolution and a better reduction of the side lobes can either be obtained if the steering vector is calibrated perfectly, or, if the Capon beamformer is extended in such a way that the unknown true steering vector $\mathbf{a}$ is estimated along with the power P_C. Li et al. [6] and Stoica et al. [7] have proposed such a robust version of the Capon beamformer that can still be solved in an efficient manner. Their approach has been used in this paper for robust Capon beamforming and in the following we indicate the steps to compute the robust Capon beamformer, which is found by solving the following expression [6]

$$\max_{\mathbf{a},P_C} P_C \quad \text{subject to} \quad \mathbf{R} - P_C \mathbf{aa}^H \qquad (2)$$

$$(\mathbf{a} - \bar{\mathbf{a}})^H \mathbf{C}^{-1} (\mathbf{a} - \bar{\mathbf{a}}) \leq 1. \quad (3)$$

Using (1) the fact that $P_C = \frac{1}{\mathbf{a}^H \mathbf{R}^{-1} \mathbf{a}}$, maximizing P_C is equivalent to minimizing $\mathbf{a}^H \mathbf{R}^{-1} \mathbf{a}$, and (2) assuming that $\mathbf{a} = 0$ is not part of the uncertainty ellipsoid — i.e. the solution to $\mathbf{a}$ will lie on the boundary of the ellipsoid — and further (3) as there is not sufficient a priori information about the variance of the individual components of the steering vector the covariance matrix $\mathbf{C}$ is set to $\mathbf{C} = \epsilon \mathbf{I}$ and the estimation
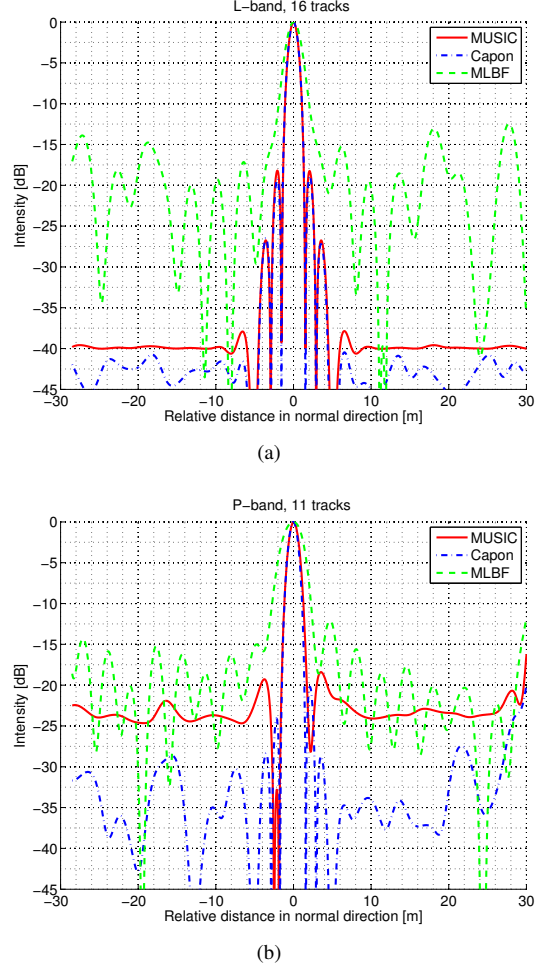
Fig. 2. Impulse response obtained from an in-scene trihedral reflector.

problem reduces to the following quadratic problem with a quadratic equality constraint

$$\min_{\mathbf{a}} \mathbf{a}^H \mathbf{R}^{-1} \mathbf{a} \qquad \text{subject to } \|\mathbf{a} - \bar{\mathbf{a}}\|^2 = \epsilon. \qquad (4)$$

The expression (4) can then be solved efficiently by using the Lagrange multiplier approach

$$F(\mathbf{a}, \lambda) = \mathbf{a}^H \mathbf{R}^{-1} \mathbf{a} + \lambda \cdot \left(\|\mathbf{a} - \bar{\mathbf{a}}\|^2 - \epsilon \right). \qquad (5)$$

The computation of the robust Capon beamformer consists of the following steps:
(1) Determine the eigen-decomposition of the sample covariance matrix $\mathbf{R} = \mathbf{UDU}^H$ and set $\mathbf{b} = \mathbf{U}^H \bar{\mathbf{a}}$.
(2) Solve $\sum_{m=1}^{K} \frac{|b_m|^2}{(1+\lambda\gamma_m)^2} = \epsilon$ for the Lagrange multiplier λ, given the fact, that there is a unique solution in the interval $[\lambda_{low}, \lambda_{up}]$ [see [8]], where

$$\lambda_{low} = \frac{\|\bar{\mathbf{a}}\| - \sqrt{\epsilon}}{\gamma_1 \sqrt{\epsilon}}, \lambda_{up} = \frac{\|\bar{\mathbf{a}}\| - \sqrt{\epsilon}}{\gamma_K \sqrt{\epsilon}} \qquad (6)$$

151

(a) MLBF, L-band

(b) RCB, L-band

(c) MUSIC, L-band

(d) Pauli decomp., L-band

(e) MLBF, P-band

(f) RCB, P-band

(g) MUSIC, P-band

(h) Pauli decomp., P-band
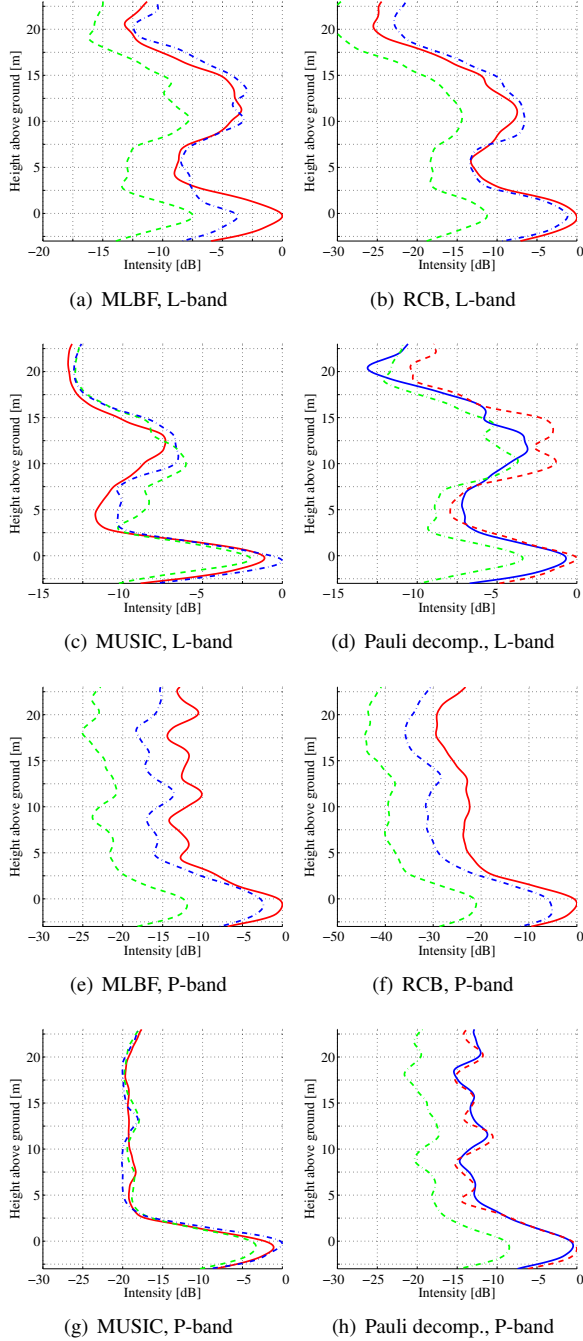
Fig. 3. Vertical profiles of relative intensities from L- and P-band tomographic data averaged over a circular sample plot of 300m^2 for the polarimetric channels HH (——), HV (——), and VV (·—), MLBF, RCB, and MUSIC, as well as the Pauli-basis HH+VV (——), HH-VV (——), and 2*HV (·—) obtained from MLBF.

(3) Calculate an estimate $\hat{\mathbf{a}}$ of the unknown steering vector $\mathbf{a}$, $\hat{\mathbf{a}} = \bar{\mathbf{a}} - \mathbf{U}(\mathbf{I} + \lambda\mathbf{D})^{-1}\mathbf{b}$.

(4) Using the knowledge that the true steering vector $\mathbf{a}$ sat-
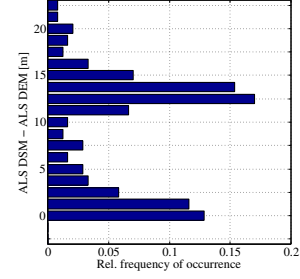
Fig. 4. Distribution of tree heights occurring within the sample plot as estimated by the histogram of height differences between the ALS DSM and the ALS DEM.

isfies the condition $\mathbf{a}^H\mathbf{a} = K$ the estimated power finally yields [8]

$$\hat{P}_C = \frac{\hat{\mathbf{a}}^H\hat{\mathbf{a}}}{K\hat{\mathbf{a}}^H\mathbf{U}\boldsymbol{\Gamma}^{-1}\mathbf{U}^H\hat{\mathbf{a}}}. \qquad (7)$$

The term $\frac{\hat{\mathbf{a}}^H\hat{\mathbf{a}}}{K}$ is necessary to get rid of a scaling ambiguity in the signal covariance term $P_C\mathbf{a}\mathbf{a}^H$ of (2) in the sense that each pair P_C/μ, $\sqrt{\mu}\mathbf{a}$, for any $\mu > 0$, yields the same covariance term [8].

3. RESULTS

In Fig. 1, a full three-dimensional voxel image of the forest is shown, obtained by focusing the L-band tomographic data set by means of the MUSIC beamformer. The impulse responses obtained from a trihedral reflector using three different approaches (MLBF, RCB, and MUSIC beamforming) to focus the MB data in the normal direction are shown in Fig. 2. In Fig. 3, vertical profiles of relative intensities obtained by averaging the focused tomographic data over a circular sample plot of 300m^2 are depicted. Profile plots are given for the polarimetric channels HH, HV, and VV, for the three beamforming techniques used for focusing in the normal direction, MLBF, RCB, and MUSIC, as well as for the Pauli basis. For comparison, histograms of the difference between a DSM and a DEM obtained from airborne laser scanning were calculated, which are used as a cross-reference estimate of tree heights occurring within a sample plot. The histogram is shown in Fig. 4. In Fig. 5, an entropy/α scatter plot is depicted for different horizontal layers at 0m (red), 5m (green), 10m (blue), and 15m (black) above ground.

4. DISCUSSION

We have successfully focused tomographic 3D SAR images of a forested area (400m x 900m) obtained from airborne multibaseline SAR data at L-band and P-band using three techniques, (1) multilook beamforming, (2) robust Capon beamforming, and (3) MUSIC for the focusing in the normal direction. The tomographic 3D voxel image of the forested

(a) L-band   (b) P-band
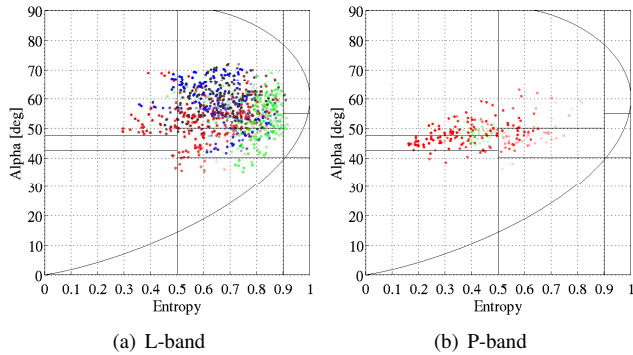
Fig. 5. Entropy/α scatter plot for different horizontal slices centered at 0m (red), 5m (green), 10m (blue), 15m (black) above ground (using the ALS-derived DEM as a reference). The entropy/α data points of each slice are plotted using transparency scaling based on the sum of the eigenvalues of the **T3** coherence matrix: 0dB $\rightarrow$ opaque, $\leq$-25dB $\rightarrow$ transparent.

area features an unprecedented level of detail (see Fig. 1). For instance, gaps in the canopy due to features like small forest roads of a width of a few meters only are clearly visible at the given ground range/azimuth resolution.

Excerpts of a detailed analysis of the focused polarimetric 3D SAR data sets, for the first time at both frequencies L-band and P-band, were presented: At L-band, main back-scattering contributions are observed at both the ground level and around the tree top region. RCB and MUSIC beamforming based vertical profiles exhibit a more distinct tomographic image by increasing the signal-to-clutter ratio and the resolution in normal direction. Thus, in order to just detect the location of the main back-scattering contributions they provide an improved performance compared to MLBF. At L-band, coherent back-scattering from the canopy (mostly in the tree-top region) is present in all polarization channels, whereas at P-band, the canopy of the forest under study is virtually transparent to the microwaves. At L-band, both the forest canopy as well as the ground level are detected (see Fig. 3). Somewhat unexpectedly, at P-band, the main scattering within the forest occurs at the ground level not only in the HH and VV channels, but *also in the cross-polarized channels*. The same behavior was also observed by Tebaldini et al. [9] for a different P-band data set.

Within the forest, surface scattering is very limited even at L-band. Interestingly, the entropy/α back-scattering classification does not change much as a function of height within the forest volume at L-band. Thus, back-scattering sources at ground level and within the canopy layer are not necessarily distinguishable only by their polarimetric signature.

6. REFERENCES

[1] O. Frey, F. Morsdorf, and E. Meier, "Tomographic imaging of a forested area by airborne multi-baseline P-band SAR," *Sensors, Special Issue on Synthetic Aperture Radar*, vol. 8, no. 9, pp. 5884–5896, Sept. 2008.

[2] O. Frey, C. Magnard, M. Rüegg, and E. Meier, "Focusing of airborne synthetic aperture radar data from highly non-linear flight tracks," *IEEE Trans. Geosci. Remote Sens.*, vol. 47, no. 6, pp. 1844–1858, June 2009.

[3] O. Frey and E. Meier, "Combining time-domain back-projection and Capon beamforming for tomographic SAR processing," in *Proc. IEEE Int. Geosci. and Remote Sens. Symp.*, 2008, pp. 445–448.

[4] R. O. Schmidt, "Multiple emitter location and signal parameter estimation," *IEEE Transactions on Antennas and Propagation*, vol. 34, no. 3, pp. 276–280, Mar. 1986.

[5] P. Stoica, Z. Wang, and J. Li, "Extended derivations of MUSIC in the presence of steering vector errors," *IEEE Trans. Signal Process.*, vol. 53, no. 3, pp. 1209–1211, Mar. 2005.

[6] J. Li, P. Stoica, and Z. Wang, "On robust Capon beamforming and diagonal loading," *IEEE Trans. Signal Process.*, vol. 51, no. 7, pp. 1702–1715, 2003.

[7] P. Stoica, Z. Wang, and J. Li, "Robust Capon beamforming," *IEEE Signal Processing Letters*, vol. 10, no. 6, pp. 172–175, June 2003.

[8] P. Stoica and R. L. Moses, *Spectral Analysis of Signals*. Upper Saddle River, NJ: Prentice Hall, 2005.

[9] S. Tebaldini, F. Rocca, and A. Monti-Guarnieri, "Model based SAR tomography of forested areas," in *Proc. IEEE Int. Geosci. and Remote Sens. Symp.*, vol. 2, July 2008, pp. 593–596.